Elemental distribution in a $Cu(In,Ga)Se_2$ solar cell at the nanoscale studied by X-ray fluorescence tomography

Report on summer project at DESY 2018

Rachel Kealy
University of Oxford
United Kingdom

Supervisor: Dr Michael Stuckelberger

Wednesday 5th September, 2018

Acknowledgements

Firstly, I would like to express my gratitude to the co-ordinators of the DESY summer student programme for organising such an enriching programme and giving me the opportunity to take part in it. I must also thank my supervisor, Michael, alongside my co-workers Christina and Liza, and the rest of the group for their collective support and guidance throughout this project. Finally, I want to thank the rest of the Summies of 2018 (with a special mention to the members of the kitchen in 32a) for being such a lovely, friendly, funny group of people with whom I now share some great memories.

Contents

1 Introduction

1.1 Motivations for solar energy

Human activity since the industrial revolution in western countries has correlated to a dramatic rise in CO_2 emissions which is now causing climate change effects, including an increasing average global temperature [1]. The threats posed by anthropogenic climate change are severe and global efforts to curtail these effects focus on reducing CO_2 emissions.

The Paris Agreement, supported by the European Union and other developed countries, details the goal of maintaining global temperatures to well below 2 °C above pre-industrial levels. To achieve this they propose a 40% reduction in the use of fossil fuels of each country by 2030 [2]. A quarter of all global CO_2 emissions come directly from the burning of fossil fuels to produce heat and electricity [3]. To reduce these emissions whilst also maintaining our current lifestyles we need to secure sustainable, equitable, and reliable energy sources. Solar photovoltaic (PV) energy promises to provide exactly this.

The sun insolates the earth with approximately 885 million TWh of energy every year, of which currently 415 GW (global cumulative installation) is harnessed globally using PV installations [4,5]. Solar energy is a sector which is growing rapidly, with a compound annual growth rate of 24% between the years 2010 and 2017 [5]. Most current installations are silicon based, however thin film technologies present a significant fraction of the market, see figure 1. Thin film solar cells are made of strongly absorbing, direct band-gap materials and thus can be made with a thickness approximately two orders of magnitude less than a typical silicon based cell. This presents unique benefits including lightweight devices on flexible substrates and the possibility of roll-to-roll manufacturing technology [6].

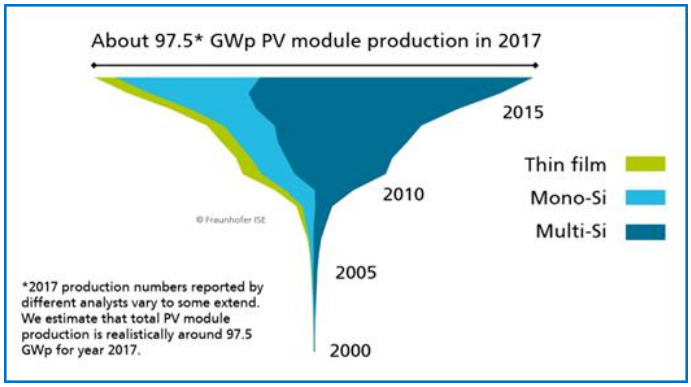

Figure 1: Schematic to highlight the dominance of silicon technologies in global PV market [5] .

1.2 CIGS thin film solar cells

There are currently three main types of inorganic thin film cell: hydrogenated amorphous silicon (a:Si:H), cadmium telluride (CdTe), and copper indium gallium diselenide (Cu(In,Ga)Se_2 or CIGS) cells. In this report we will study a sample of high efficiency CIGS cell. The charge separation and collection properties required to make an effective solar cell are achieved through a band structure attained by stacking different materials as shown in figure 2.

The first base layer of the structure is the substrate. This may be glass, which is useful for its smooth surface and high temperature stability, or it could be a flexible substrate such as a polymer or stainless steel foil. A Mo layer is typically deposited on top of this, which is useful as an electrical back contact as well as providing a diffusion barrier between the substrate and the subsequent deposited layers [7]. A p-type absorber layer of a CIGS quaternary alloy is then deposited and can be deposited by a variety of manufacturing techniques. The layer is p-type doped due to the presence of intrinsic defects arising from deviation from stoichiometry; it is typically deficient in Cu. A thin CdS buffer layer is then deposited and finally a transparent conducting oxide layer (TCO) is added to provide the electrical contact at the front surface. This TCO can be made up of layers of intrinsic and then Al-doped ZnO [8].

Whilst the theoretical efficiency limit of a CIGS cell is 29%, the best cells produced are only reaching efficiencies of about 22.6% and modules perform in the range 13- 15% [9]. The performance of a solar cell is dictated by its weakest parts and thus it seems clear that CIGS is limited by its electrically poorest performing regions. It is expected that localised compositional inhomogeneities correlate to areas of solar cell with poor electrical performance and it is these electrically defective areas that weaken the efficiency of the entire module.

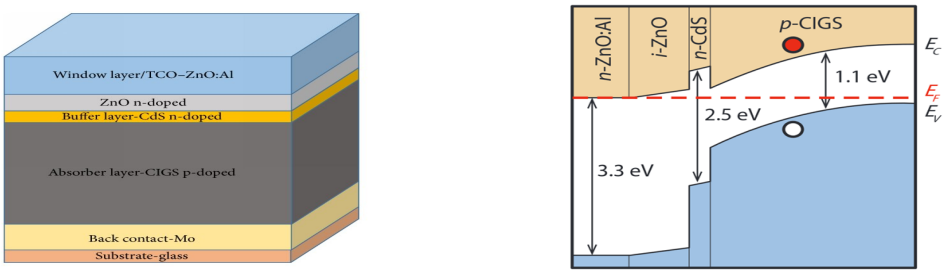

(a) Layered structure [10]

(b) Band structure [8]

Figure 2: Figure shows the structure of a typical CIGS cell alongside the corresponding band structure

1.3 Synchrotron X-ray research into CIGS PV material

Many experimental techniques have been used to investigate the spatial distribution of elements within CIGS thin film cells. Studies using secondary ion mass spectroscopy (SIMS), Auger electron spectroscopy (AES), and atom probe tomography (APT) have all provided compositional information elucidating depth profiles or detailed atomic scale reconstruction of composition within microstructural features [9, 11, 12]. Correlative studies pair such compositional data with data on cell performance using methods such as light or X-ray beam induced current (LBIC or XBIC) to test if underperforming areas correspond to compositional inhomogeneity [9, 13].

Hard X-rays, such as those produced by synchrotrons, offer invaluable properties in the field of photovoltaics research. They are highly penetrating, enabling the study of layered structures, and can be focused down to extremely small probes on the scale of 50 nm and potentially even further [13]. Furthermore, synchrotron radiation is highly brilliant with $\Delta E/E \approx 10^{-4}$ and thus a high-flux X-ray beam with extremely narrow bandwidth can be scanned over the sample to provide a detailed compositional map of the material it is incident upon [14]. These properties make X-rays suitable for analysis of CIGS solar cell material, as they are able to penetrate through capping layers and multiple interfaces to reveal buried structure.

One method of studying samples of PV materials with X-rays is X-ray fluorescence (XRF) tomography. Fluorescence refers to one of the processes resulting from X-ray irradiation of matter. An incident X-ray has sufficient energy to excite an electron from an inner orbital of an atom leaving a "hole" in the electronic structure into which another higher energy electron may fall. This electronic transition reduces the energy of the electron system and this reduction in energy is compensated by generation of an X-ray photon of the same energy. As the precise electronic structure is unique to each element, the energy of the produced X-ray photons is similarly characteristic of the element. Thus, from each scanned point a spectrum can be obtained providing relative intensities of different elements present [15].

2 Method

2.1 Sample preparation

The sample was taken from a high efficiency CIGS solar cell manufactured by roll to roll processing on a stainless steel substrate. Flakes were peeled off the cell to produce small pieces suitable for cutting down to size using a Ga focused ion beam (FIB). After FIB processing the sample appears to have a triangular wedge shape about 6 µm in length and approximately 3 µm in thickness. The final sample does not include the steel substrate upon which it was originally deposited. Figure 3 shows the evolution of the sample through this process.

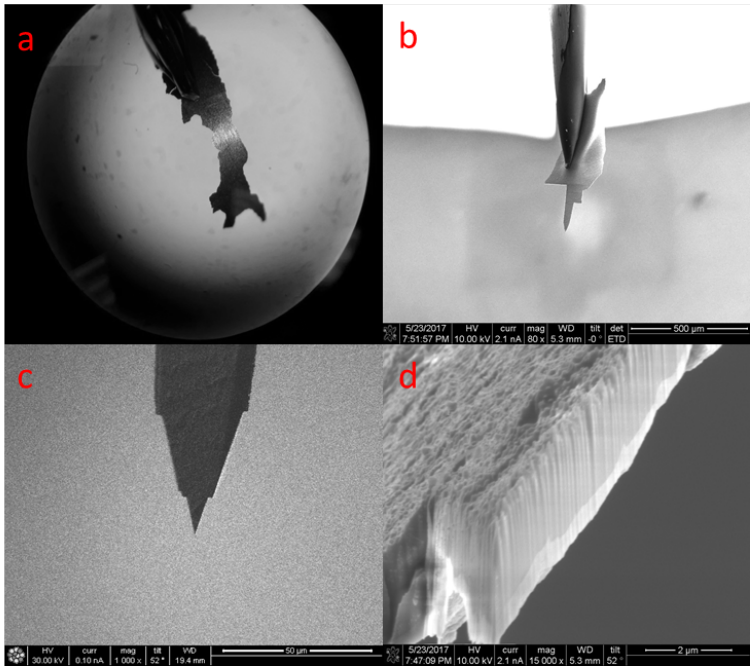

Figure 3: Images of the CIGS sample measured in this report. a) Image of flake peeled off CIGS sample, b) SEM image of flake on needle for FIB, c) Image from FIB of the sample, d) Zoomed SEM image of tip. Courtesy of B. West

2.2 XRF tomographic measurement

The HXN beamline (Brookhaven National Laboratory, USA) was used to take the nanoprobe X-ray fluorescence tomography measurements at 10.4 keV just above the K absorption edge of Ga [16]. The X-ray probe is focused down to the nanoscale using X-ray zone plate optics. The sample is rotated and translated in space so that effectively a raster of XRF measurements are taken. The set up for this process is illustrated in figure 4. From these measurements a tomographic reconstruction can take place which allows the data to be understood in 3D.

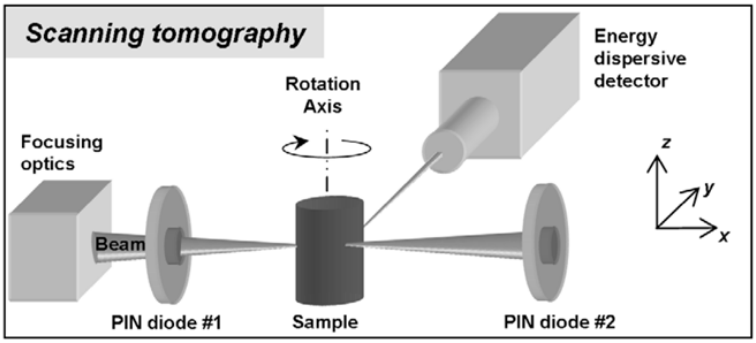

Figure 4: Schematic to show the process of X-ray tomography with a nanoprobe [14]

2.3 Analysis of data

The data after tomographic reconstruction is plotted in python and Mayavi. In this work the 3D representations of the sample are shown with spherical, coloured glyphs with each glyph representing a voxel and the colour pertaining to relative content of a given element. These plots can be used to visualise the 3D structure of the sample, and internal structure can be revealed by plotting the 3D bulk with translucent glyphs alongside opaque glyphs of the element of interest. In the x and y directions data points are 56 nm apart and in the z direction they are 84 nm apart.

To understand the elemental distribution throughout the 3D sample, we have developed the sampling method indicated in figure 5. The co-ordinate system is first rotated so that the growth direction of the sample wedge is parallel to the new z-axis. We then define a cylinder of chosen position and radius with its rotation axis along the new z-axis. This cylinder which we have cut out is our sample cylinder and we can use it to measure elemental distribution through the wedge in one location. It is further cut into thin slices (generally 70 – 100 nm thick).

Once the sample cylinder has been sliced into thin pieces, we want to find the amount of each element within the piece. We can do this by simply summing the contents of all the voxels in that piece and returning this value as the content for that piece. However we find this approach gives a strong periodic noise on top of the data. This noise is explained as the disparity in voxel number from piece to piece, which arises from misalignment of the new coordinate system in which we define the slices and the original voxel grid. This means that periodically the pieces contain more and then less voxels which is a noticeable effect when the slices are thin. To avoid this noise, the simple solution is to normalise the total contents of a slice by the number of voxels it contains. This appears to remove the noise, as shown in figure 6.

This process is then repeated in multiple locations across the sample. The cylinder is effectively rastered over as many points as desired and this can be used to build up an idea of how elemental distribution varies across the entire sample.

Finally, with a suitable range of points to sample chosen, we can raster the sampling cylinder across the surface and obtain subplots with the composition profiles at each position. This can be achieved for the cylinder lying in any of the planes shown above and for any list of elements of interest. Figure 8 shows how a raster scan over a relatively small area produces a set of subplots.

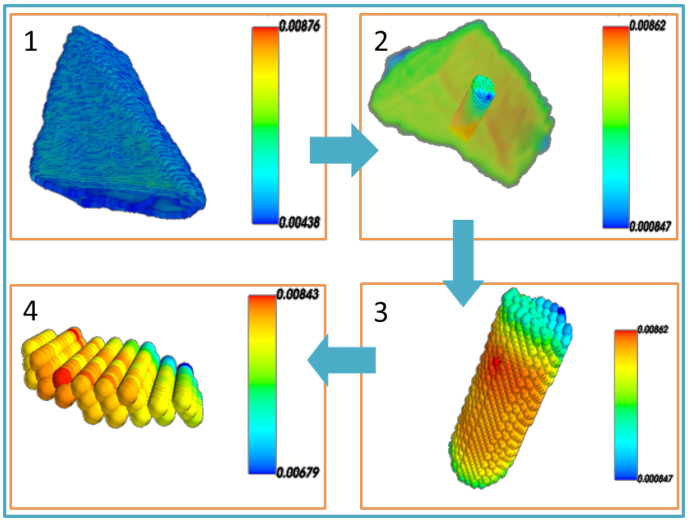

Figure 5: Schematic to demonstrate the four-stage process used to sample elemental distribution across the sample. In stage 1 the 3D volume is plotted and then in stage 2 a cylidner is defined and "cut-out" in stage 3. In stage 4 this cylinder is then cut into thin slices for analysis. The colour bar here is scaled by the measured intensity of copper.

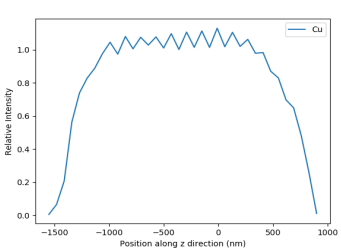

(a) Total content of each slice is used

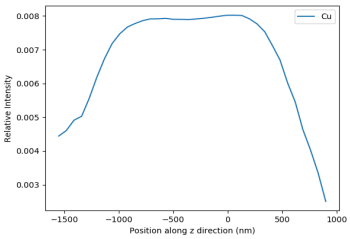

(b) Total content divided by voxel number of each slice is used

Figure 6: Figure to show that periodic noise arises when the voxel count of each slice is not accounted for.

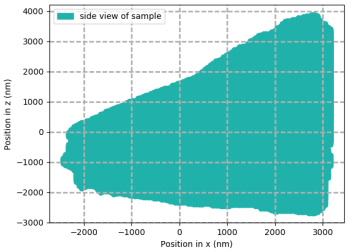

(a) xy plane projection

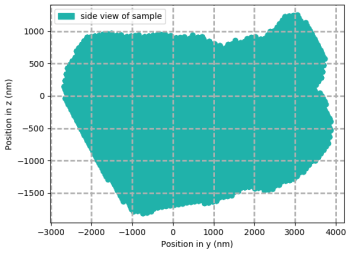

(b) y-z plane projection

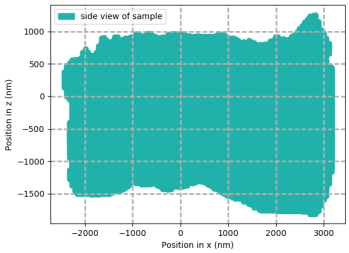

(c) x-z plane projection

Figure 7: Figure shows

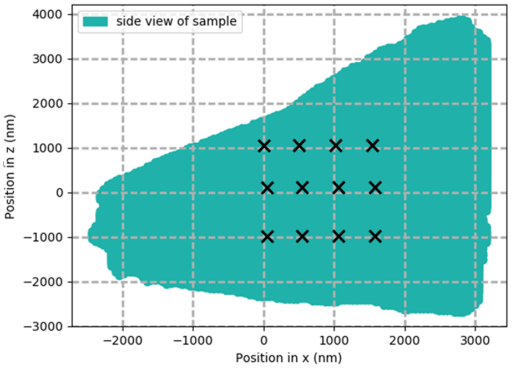

(a) Position map with sampling points indicated

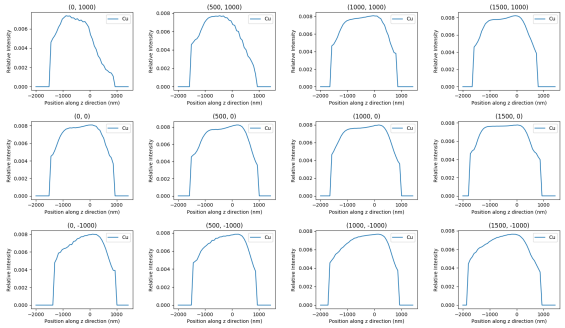

(b) Subplots obtained from each position

Figure 8: Figure to show how a raster scan of the sampling cylinder produces a set of subplots

3 Results

3.1 Elemental distribution throughout sample

We first plot the elemental distribution along the growth axis for a sample cylinder with a radius that extends beyond the edges of the sample (thus sampling the entire contents of the cylinder). The result of this is shown in figure 9.

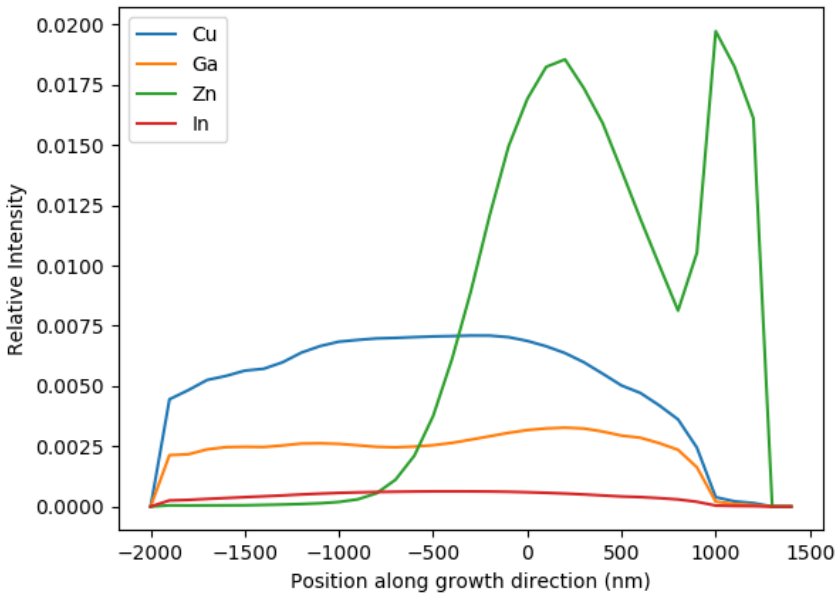

Figure 9: The intensity of the signal from each element along the growth direction using a sampling cylinder with radius of 6000 nm (thus spanning the whole sample)located at (0,0) in the x-y plane

The first thing to note is that only four elements (Cu, In, Ga, and Zn) are visible in the plot, even though we also have identified the presence of several others (namely Cd, Cr, Fe, Ni, P, and Se). Simply, these elements are not seen in such a plot, because signal intensity for a given element is a function of both X-ray energy used and concentration. In CIGS the Cu and Ga are the main components of the absorber and a large amount of Zn is present because of the TCO at the top of the sample. The X-ray energy used was 10.4 keV which meant that Cu, Ga, and Zn could be measured at high sensitivity from K lines. However at this energy only In L edges can be measured at mediocre sensitivity and Se, which should be seen in high concentration in the absorber, is hardly detectable because of the low energy Se L lines.

We note that In,Ga,Cu follow a comparable shape, which is expected due to co-presence in the bulk, whereas Zn follows a distinct shape. We assume the Zn is solely present from deposition of the TCO onto the absorber. The double-peaked appearance is probably an artifact of the uneven surface topology of the wedge meaning that the top of the sample effectively starts at different z-values in

different places across the sample. We repeat this plot for elemental distribution from the same position, but with a radius of only 100 nm (thus sampling only a small fraction of the sample over which the surface topology should not significantly change). This is presented in figure 10.

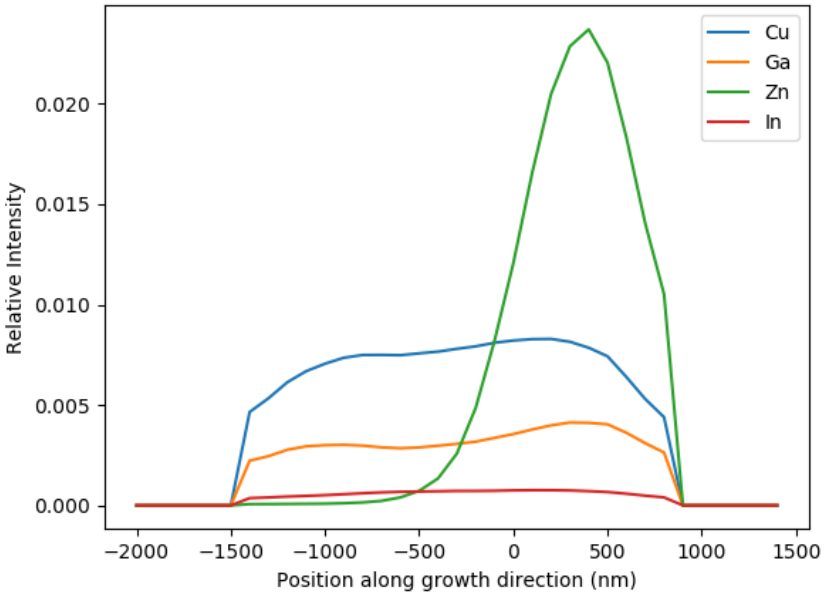

Figure 10: Graph to show the intensity of the signal from each element along the growth direction using a sampling cylinder with radius of 6000 nm (thus spanning the whole sample)located at (0,0) in the x-y plane

From figure 10 we see that even when localized to a couple of hundred nanometers, either the topology of the Zn-rich layer varies a lot, or Zn has diffused significantly into the sample. In the future we should check which of these is true. We do however note that there is now only one peak as expected. In both figures 9 and 10 we see that the Cu, Ga, and In intensities remain present throughout the thickness of the sample (as expected) however do seem to vary long the growth direction. The variation in proportion of Cu, Ga, and In across the sample is presented later in this report.

To see how elemental distribution may vary across the sample we can use sampling cylinders as used to generate figure 10 all across the surface of the sample. The results are presented in figure 12. The plots correspond to points in the x-y plane as shown in figure 7.

Over the 4 μm^2 region plotted the sample is inhomogeneous. In particular we notice dips in all elements at certain points along the z-axis. This may be very close to the surface, where the uneven topology in edge regions means that in certain slices some voxels are sampled, and others they aren't. However we also notice dips in all elements further into the bulk, which may be explained as voids in the material. Further such "void candidates" are discussed later.

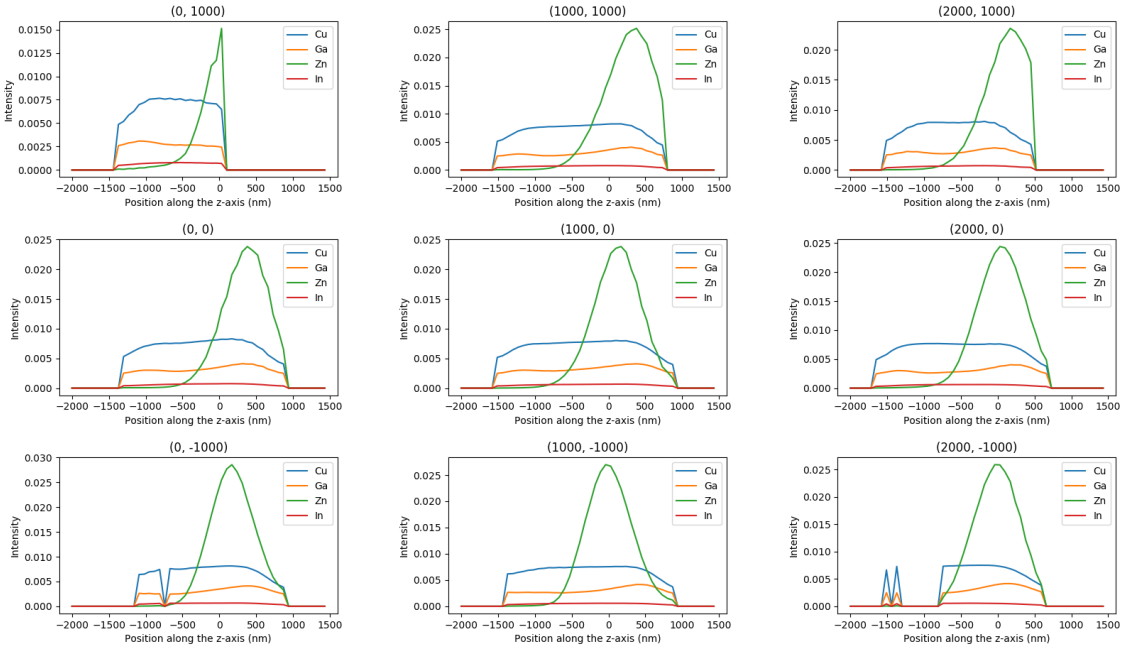

Figure 11: Subplots show element concentration along the growth direction in sampling cylinders arranged over the central region of the sample at co-ordinates (X,Y). Using a cylinder with radius of 200 nm, and sliced every 70nm

3.2 Gallium damage at surfaces

The sample was cut to size using a focused ion beam of Ga. We want to see if this process has introduced artifacts of gallium damage into the sides of the material we are studying. To judge if such artifacts were present we looked at the relative fraction of Ga (specifically, $\frac{Ga}{Ga+Cu}$) along the x and y directions over a range of positions all across the surfaces. To do this we adapted the process described in the method so that the sampling cylinder was defined to have its axis along either the x or y direction as shown in figure 12.

The results of these measurements are shown in figures 13-14. It is readily apparent that over the areas scanned, there are generally distinct peaks either at the front or back or both of the sample. This suggests that at each surface of the sample there is an enriched Ga layer about 100 nm thick, probably introduced by FIB processing. It is interesting that these peaks are not observed over the entirety of the surface sampled and suggests that the Ga damage is inhomogeneous.

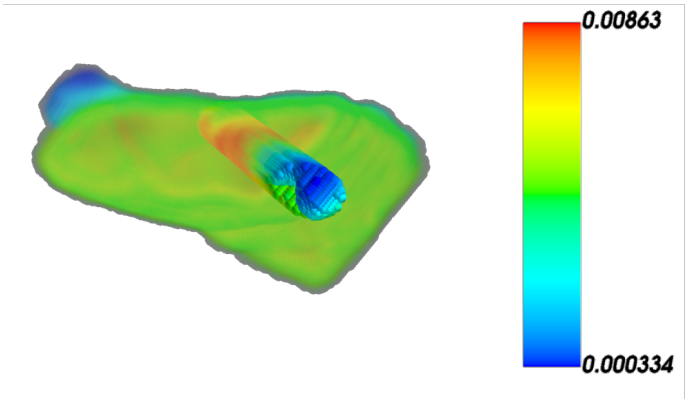

Figure 12: 3D plot to show the sampling cylinder drilled into the side of the wedge so that its axis is parallel to the y-direction

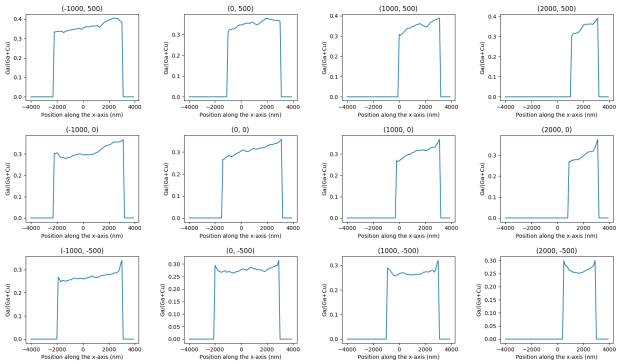

Figure 13: Subplots to show how the relative percentage of Ga in the bulk varies along the x-direction

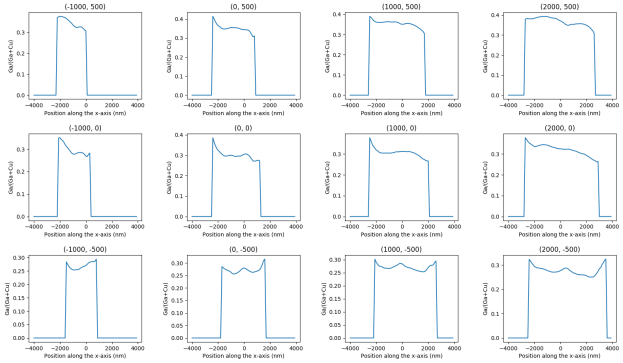

Figure 14: Subplots to show how the relative percentage of Ga in the bulk varies along the y-direction

3.3 Proportion of Cu, Ga, and In through bulk

Looking at CIGS in the context of a semiconductor material with applications in PV, we are interested to understand the variation in concentration of Cu, Ga and In through the bulk (Se is not included in our analysis due to its very weak signal). From measured concentration gradients we should be able to calculate band structure through the material. This is outside the scope of this report as first the signal intensity must be converted into concentration. Instead, in figure 15 we show the fractions of Cu/Ga and Ga/In which give us some insight into how the concentration of these elements varies through the material.

It is observed that the Ga/In ratio dips in the center of the bulk, which is consistent with Ga doping being higher at the front and back surfaces to improve charge carrier collection efficiency. The Cu/Ga ratio is seen to be quite flat across the sample.

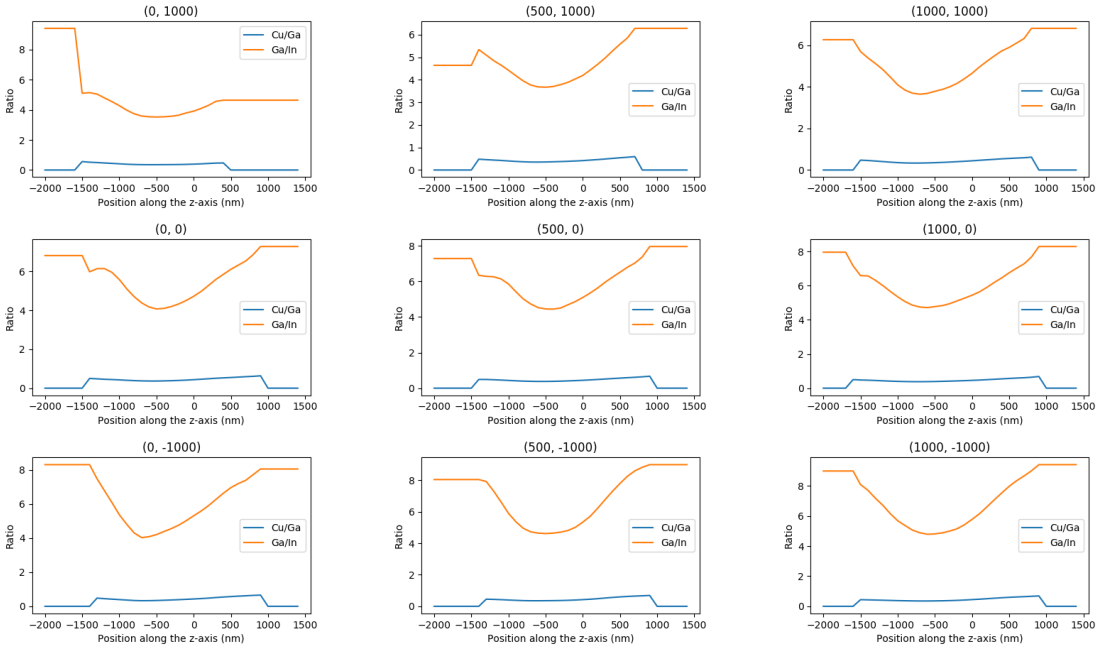

Figure 15: Subplots to show how the fractions Cu/Ga and Ga/In vary along the growth direction of the sample. A sample cylinder of radius 400 nm was used to measure over the x-y plane

3.4 Further work

In some sampling locations the plots of elemental distribution show a sudden drop in intensity for all elements at z-values which appear to lie within the bulk of the material. This implies that for some slices ,which should be in the middle of the material, there are none of the measured elements present and thus there is a void. Some examples of such "void candidates" are presented in figure 16.

Plotting the Cu of the sample as a translucent matrix and then plotting on top of this another element where it exceeds a significant threshold value has given us further insight into the distribution of trace elements in the material. For example both Fe and Ni appear to be found in a significant quantity in the center of the bulk material- as seen in figure 17. The presence of transition metals within CIGS material is of interest to understanding electrical defects within CIGS material.

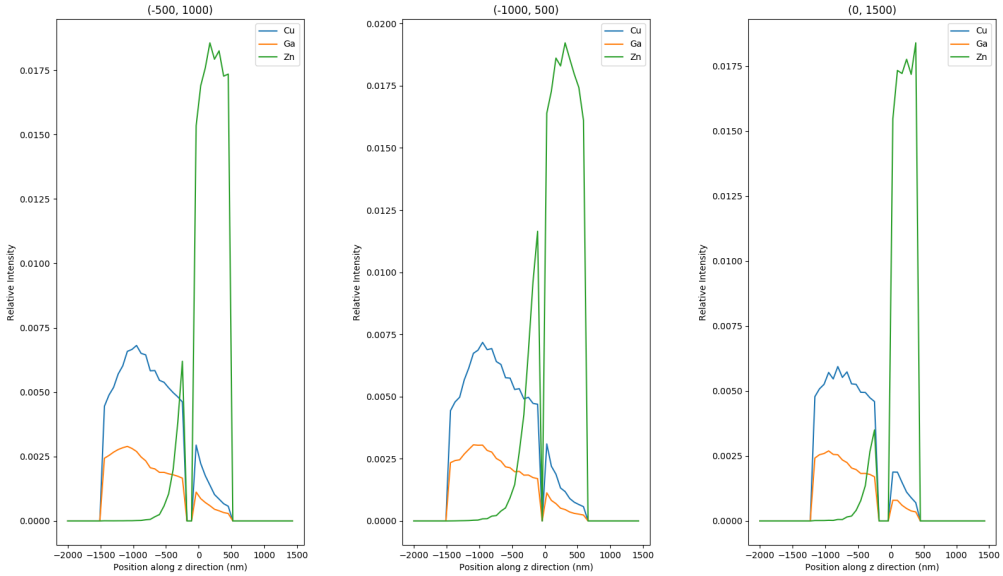

Figure 16: Subplots to show how the fractions Cu/Ga and Ga/In vary along the growth direction of the sample. A sample cylinder of radius 400 nm was used to measure over the x-y plane

(a) [Ni] above 0.8*max

(b) [Fe] above 0.5*max

Figure 17: Transition elements with intensities measured above defined thresholds are highlighted within the bulk material

4 Conclusions

Through this work we have developed the basis of a method for sampling elemental distribution through a 3D volume of CIGS material. We have used the technique to observe expected features. For example, we have found that the sample we have confirmed the layered structure of the CIGS cell and propose linking the width of the observed Zn peak to an uneven surface topology. Furthermore we have found evidence of inhomogeneous Ga damage possibly at depths of up to 100 nm into the sides of the sample. We hope to build on these results with more rigorous quantitative analysis and present the results in a more visually compelling manner in future work. Analysis has also revealed further features of interest, in particular the possibility of voids and transition metals within the bulk absorber, and these also should be investigated.

The results presented here and those of future analysis should be used both to deepen our understanding of the nanocomposition of CIGS cells and to inform our processing routes for their manufacture. In this way we can work towards developing more efficient CIGS cells and thus continue to pave the way for a future powered with renewable energy.

References

[1] D. Wuebbles, D. Fahey, K. Hibbard, D. Dokken, B. Stewart, and T. Maycock, "Climate science special report: Fourth national climate assessment," tech. rep., U.S. Global Change Research Program, Washington, DC, USA, 2017.

[2] "Communication from the commission to the european parliament and the council, the road from paris: assessing the implications of the paris agreement and accompanying the proposal for a council decision on the signing, on behalf of the european union, of the paris agreement adopted under the united nations framework convention on climate change," tech. rep., European Commission, Brussels, 2016.

[3] O. Edenhofer, R. Pichs-Madruga, Y. Sokona, E. Farahani, S. Kadner, K. Seyboth, A. Adler, I. Baum, S. Brunne, P. Eickemeier, B. Kriemann, J. Savolainen, S. Schlömer, C. von Stechow, T. Zwickel, and J. Minx, "Climate change 2014: Mitigation of climate change. contribution of working group iii to the fifth assessment report of the intergovernmental panel on climate change," tech. rep., Cambridge University Press, Cambridge, United Kingdom and New York, NY, USA., 2014. IPCC.

[4] I. E. Agency, "Technology roadmap: Solar photovoltaic energy, 2014 edition," tech. rep., IEA publications, IEA publications 9, rue de la Fédération, 75739 PARIS CEDEX 15., 2014.

[5] "Photovoltaics report," tech. rep., Fraunhofer Institute for Solar Energy Systems, ISE with support of PSE Conferences & Consulting GmbH, 2018.

[6] T. D. Lee and A. U. Ebong, "A review of thin film solar cell technolgies and challenges," *Renewable and Sustainable Energy Reviews*, vol. 70, pp. 1286–1297, 2017.

[7] A. C. P. Blösch, F. Pianezzi, "Diffusion barrier properties of molybdenum back contacts for cu(in,ga)se 2 solar cells on stainless steel foils," *Journal of Applied Physics*, vol. 113, no. 5, 2013.

[8] A. Smets, K. Jäger, O. Isabella, R. V. Swaij, and M. Zeman, *Solar Energy: The physics and engineering of photovoltaic conversion technologies and systems*. Cambridge, CB4 1CQ, England: UIT Cambridge, 1 ed., 2016.

[9] L. Mansfield, R. L. Garris, S. Johnston, J. V. Li, H. L. Guthrye, and K. Ramanthan, "Electrical characterization and comparison of cigs solar cells made with different structures and fabrication techniques," *Solar Energy Materials & Solar Cells*, vol. 174, pp. 77–83, 2018.

[10] A. Parisi, R. Pernice, V. Rocca, L. Curcio, S. Stiuala, and A. C. Cino, "Graded carrier concentration absorber profile for high efficiency cigs solar cells," *International Journal of Photoenergy*, 2015.

[11] J. Lee, S. H. Kim, and Y. Lee, "Quantitive analyses of photovoltaic cigs thin films via sims depth profiling with elemental ions and mcs clusters," *European Applications of Surface and Interface Analysis*, vol. 46, no. 11, 2014.

[12] M. Raghuwanshi, *Influence of Grain Boundary Chemistry on the properties of CIGS photovoltaic cells*. PhD thesis, University of Rouen, 2015.

[13] M. Stuckelberger, B. West, T. Nietzold, B. Lai, J. M. Maser, V. Rose, and M. L. Bertoni, "Engineering solar cells based on correlative x-ray microscopy," *Journal of Materials Research*, vol. 32, no. 10, pp. 1825–1854, 2017.

[14] P. Bleuet, P. Gergaud, L. Lemelle, and A. S. Simionovici, "3d chemical imaging based on a third-generation synchrotron source," *TrAC Trends in Analytical Chemistry*, vol. 29, no. 6, pp. 518–527, 2010.

[15] S.-K. Son, "Lecture series: Fundamentals of x-ray interaction with matter," August 2018.

[16] E. Nazaretski, K. Lauer, H. Yan, N. Bouet, J. Zhou, R. Conley, X. Huang, W. Xu, M. Lu, K. Gofron, S. Kalbfleisch, U. Wagner, C. Rau, and Y. Chu, "Pushing the limits: An instrument for hard x-ray imaging below 20 nm," *Journal of Synchrotron Radiation*, vol. 22, no. 2, 2015.